Generative MIMO Beam Map Construction for Location Recovery and Beam Tracking

Wangqian Chen, Junting Chen, Member, IEEE, and Shuguang Cui, Fellow, IEEE

Abstract-Machine learning (ML) has greatly advanced datadriven channel modeling and resource optimization in wireless communication systems. However, most existing ML-based methods rely on large, accurately labeled datasets with location information, which are often difficult and costly to obtain. This paper proposes a generative framework to recover location labels directly from sequences of sparse channel state information (CSI) measurements, without explicit location labels for radio map construction. Instead of directly storing raw CSI, we learn a compact low-dimensional radio map embedding and leverage a generative model to reconstruct the high-dimensional CSI. Specifically, to address the uncertainty of sparse CSI, a dualscale feature extraction scheme is designed to enhance feature representation by jointly exploiting correlations from angular space and across neighboring samples. We develop a hybrid recurrent-convolutional encoder to learn mobility patterns, which combines a truncation strategy and multi-scale convolutions in the recurrent neural network (RNN) to ensure feature robustness against short-term fluctuations. Unlike conventional Gaussian priors in latent space, we embed a learnable radio map to capture the location information by encoding high-level positional features from CSI measurements. Finally, a diffusion-based generative decoder reconstructs the full CSI with high fidelity by conditioning on the positional features in the radio map. Numerical experiments demonstrate that the proposed model can improve localization accuracy by over 30% and achieve a 20% capacity gain in non-line-of-sight (NLOS) scenarios compared with model-based Kalman filter approaches.

Index Terms—Generative radio map, Location recovery, Blind construction, Beam tracking, Deep learning

I. INTRODUCTION

ASSIVE multiple-input multiple-output (MIMO) has emerged as a cornerstone technology for 5G and beyond due to its ability to achieve efficient spatial multiplexing, high beamforming gain, and flexible interference mitigation.

This work was supported in part by the National Science Foundation of China (NSFC) under Grant 62293482, in part by Basic Research Project under Grant HZQB-KCZYZ-2021067 of Hetao Shenzhen-HK S&T Cooperation Zone, in part by NSFC Grant 62171398, in part by Shenzhen Science and Technology Program under Grant JCYJ20220530143804010, Grant KJZD20230923115104009, and Grant KQTD20200909114730003, in part by Guangdong Basic and Applied Basic Research Foundation 2024A1515011206, in part by Guangdong Research Grant 2019QN01X895, in part by the Guangdong Provincial Key Laboratory of Future Networks of Intelligence under Grant 2022B1212010001 and Guangdong-Hong Kong-Macao Joint Laboratory for Millimeter-Wave and Terahertz under Grant 2023B1212120002, in part by the National Key R&D Program of China under Grant 2018YFB1800800, and in part by the Key Area R&D Program of Guangdong Province under Grant 2018B030338001.

W. Chen, J. Chen and S. Cui are with the School of Science and Engineering, the Shenzhen Future Network of Intelligence Institute (FNii-Shenzhen), and the Guangdong Provincial Key Laboratory of Future Networks of Intelligence, The Chinese University of Hong Kong, Shenzhen, Guangdong 518172, China (email: wangqianchen@link.cuhk.edu.cn; juntingc@cuhk.edu.cn; shuguangcui@cuhk.edu.cn).

However, to achieve the full benefit of massive MIMO, the high dimensional CSI is essential, which imposes significant channel training overhead especially under a large number of antennas. With the continued deployment of massive wireless networks, acquiring accurate CSI to ensure network connectivity and performance has become increasingly challenging in dense and dynamic environments. To this end, a channel knowledge database that incorporates radio maps as a key component has been proposed as a promising solution to provide channel knowledge of the environment [1, 2]. Specifically, radio maps enable target localization and beam alignment without exhaustive channel training [3, 4], and have been leveraged for hybrid beamforming and interference coordination to improve energy efficiency [5, 6].

The fundamental challenge of MIMO radio map construction is the demand of a large volume of location-labeled data, with each sample annotated with precision location labels. Although there have been some works on radio map construction using statistical modeling [7, 8], interpolation techniques [9, 10], tensor completion [11, 12], and deep learning frameworks [13]–[15], these approaches face the implementation challenge of requiring massive amounts of location-labeled CSI data during the radio map construction phase. Some recent advances [16, 17] in generative models attempt to synthesize radio maps directly from city maps; however, they still require real radio maps with locations for training. Even this challenge can be settled during the model training and radio map construction phase, the constructed radio map may still not be reliable, since minor inaccuracy in location labels or temporal changes in the environment can severely affect the radio map accuracy. Moreover, establishing a ground-truth reference system for data collection is not only expensive, but the dynamic nature of the wireless environment necessitates repeating such a costly measurement campaign whenever significant physical changes occur. Finally, there are escalating concerns over user location privacy, which hinders the availability of massive locationlabeled CSI data in a crowd-sourcing manner.

Ray tracing (RT) methods can bypass the need of locationlabeled CSI by constructing radio maps through simulated signal propagation, including reflection, diffraction, and scattering, without relying on labeled data [18, 19]. These methods operate by launching a multitude of virtual rays and analyzing their interactions with a detailed environmental geometry model. While RT provides detailed spatial information about CSI, the computational complexity and memory requirement for simulating the intricate signal interactions are prohibitively large. Moreover, RT relies not only on accurate environmental geometry, but also the electromagnetic properties of materials, which may not be accurately available in the network.

Channel charting (CC) is promising to circumvent the demand on labeled CSI data. It learns low-dimensional charts of CSI by preserving their local geometry in a self-supervised manner to alleviate the need of location labels [20, 21]. However, CC only captures the relative spatial relationships among samples in a latent space, and requires additional calibration to align with the physical space. To recover true locations, some approaches employed an affine transformation to align the channel chart with real-world coordinates, using a small set of newly collected CSI measurements at known locations [22]–[24]. However, this calibration step still requires accurate location information. The work in [25] proposed to leverage access point positions rather than user equipment (UE) positions by encouraging each UE to be closer to the access point from which it receives stronger power. But this approach is effective only in line-of-sight (LOS) scenarios, and its performance degrades significantly in NLOS environments with rich multipath propagation.

This paper attempts to build a radio-map-embedded generative framework for MIMO radio map construction using sequences of sparse CSI measurements without explicit location labels. Unlike many existing approaches that rely on accurately location-labeled data for calibration and radio map construction, we propose to reconstruct UE locations from sparse CSI measurements as an intermediate step to facilitate radio map reconstruction, which in turn enhances the capability of high-dimensional CSI generation, UE localization, and beam tracking. While some earlier attempt [26] employed a modelbased Kalman filter to estimate UE trajectories and CSI from coarse location information, it required the channel model to be Gaussian and the mobility model to be a Markov chain, which limits its application in realistic environments where multipath propagation may lead to non-Gaussian behavior and user mobility can be non-Markovian. Prior work [26] is also limited to short trajectory recovery as minor model mismatches (e.g., violating the Gaussian assumptions or motion models) accumulate over time and cause large estimation errors.

We propose a generative framework to recover UE trajectories from sparse, unlabeled CSI measurements, without relying on explicit mobility models or location labels. Specifically, to reduce the uncertainty of sparse CSI due to incomplete channel information, we design a dual-scale feature extraction scheme that enhances feature representation by exploiting angular correlations within each CSI snapshot and spatial correlations across neighboring samples. In particular, selfattention is utilized to model intra-snapshot angular dependencies, while multi-scale convolutions capture inter-sample spatial relationships. We develop a bidirectional RNN encoder integrated with a convolutional neural network (CNN) to learn mobility patterns from both short and long CSI sequences. A truncation strategy is employed to address the potential issue of large initial errors of the recovered trajectory, while multiscale convolutions are further applied to smooth short-term fluctuations and enhance feature robustness. We embed a radio map into the network to capture CSI knowledge for trajectory recovery. Each embedding vector in the radio map encodes low-dimensional positional features that capture the CSI distribution in a specific physical region, rather than storing highdimensional raw CSI. A diffusion-based generative decoder then reconstructs the full CSI by leveraging the positional features to achieve accurate and high-fidelity generation.

The novelty and contribution are summarized as follows:

- We propose a deep generative framework embedded with a learnable radio map for joint location recovery and MIMO beam map construction from sparse and unlabeled CSI measurements, without relying on explicit location labels for training or inference.
- We design a dual-scale feature extraction scheme to capture the angular and spatial patterns of unlabeled CSI data, which integrates self-attention and multi-scale convolutions to extract informative features from sparse CSI data and enhance feature representation.
- We develop a hybrid RNN-CNN encoder to learn mobility patterns from both short and long CSI sequences. The fundamental challenge of potentially large error at the beginning of the recovered trajectory is addressed by a proposed truncation and multi-scale convolution strategy within the bidirectional RNN structure.
- We conduct experiments to show that the proposed model improves trajectory recovery accuracy by over 30% using only one pilot per second for a UE moving at 1 m/s, and achieves on average over 98% of the perfect CSI capacity under LOS conditions for MIMO beam tracking, with over 20% capacity gain in NLOS scenarios, compared to Kalman filter based approaches.

The rest of the paper is organized as follows. Section II reviews the system model, while Section III illustrates the deep learning architecture for joint trajectory recovery and radio map construction. Design examples are presented in Section V and conclusions are drawn in Section VI.

Notations: $(\cdot)^T$ and $(\cdot)^*$ represent the transpose and Hermitian transpose operations, respectively. $|\cdot|$ denotes the absolute value and $||\cdot||$ represents the L_2 norm. \odot denotes the elementwise product, and $\mathcal{N}(\cdot,\cdot)$ denotes a Gaussian distribution.

II. SYSTEM MODEL

Consider a massive MIMO communication system with N_b base stations (BSs) and multiple mobile UEs, where each BS, treated as transmitter (TX), is equipped with N_t antennas, and all UEs, treated as receivers (RXs), are single-antenna devices. Denote a link $\tilde{\mathbf{p}} = (\mathbf{p}_t, \mathbf{p}_r) \in \mathbb{R}^6$ with the positions $\mathbf{p}_t, \mathbf{p}_r \in \mathbb{R}^3$ of the TX and the RX, respectively.

A. Channel Model and Measurement Model

A narrow-band MIMO channel of $\tilde{\mathbf{p}}$ can be modeled as

$$\mathbf{h}(\tilde{\mathbf{p}}) = \sum_{l=0}^{L} \beta_l(\tilde{\mathbf{p}}) \mathbf{a}^*(\phi_l(\tilde{\mathbf{p}}))$$
 (1)

where $\beta_l(\tilde{\mathbf{p}})$ denotes the gain of the lth propagation path, and $\mathbf{a}(\phi_l(\tilde{\mathbf{p}}))$ is the array steering vector at the angle of departure (AOD) $\phi_l(\tilde{\mathbf{p}})$ from the BS.

A codebook-based approach is applied at the BS to form MIMO beams for CSI measurements. Denote \mathbf{w}_j as the jth

beamforming vector from a predetermined codebook W with the power constrain $|\mathbf{w}_{j}^{*}\mathbf{w}_{j}| = 1$. The CSI measurement of the link $\tilde{\mathbf{p}}$ under beamforming vector \mathbf{w}_{i} is given as

$$\rho(\tilde{\mathbf{p}}, \mathbf{w}_j) = \mathbb{E}\left[\left|\mathbf{h}(\tilde{\mathbf{p}})\mathbf{w}_j\right|^2\right] + n$$
 (2)

where $\mathbb{E}[\cdot]$ denotes the expectation over the randomness of the small-scale fading, and n denotes the measurement noise.

Denote $g_{\mathbf{r}} = [\rho(\tilde{\mathbf{p}}, \mathbf{w}_1), ..., \rho(\tilde{\mathbf{p}}, \mathbf{w}_{|\mathcal{W}|})] \in \mathbb{R}^{1 \times N_b \cdot |\mathcal{W}|}$ as the full CSI vector for all the N_b BSs for the RX location $\mathbf{p}_{\mathbf{r}}$, where $|\mathcal{W}|$ denotes the number of beamforming vectors in the codebook \mathcal{W} . The sparse CSI observation is thus denoted by $\mathring{g}_{\mathbf{r}} = g_{\mathbf{r}} \odot m$, where $m \in \mathbb{R}^{1 \times N_b \cdot |\mathcal{W}|}$ is a binary mask vector whose zero entries indicate unobserved measurements.

Consider a ground mobile UE traversing an arbitrary trajectory while collecting CSI measurements along the way. At each location, some sparse CSI measurements \mathring{g}_r are taken. Denote $\mathring{\mathcal{G}}_l = (\mathring{g}_r^0, \mathring{g}_r^1, ..., \mathring{g}_r^l)$ as the sequence of collected CSI observations along the trajectory $\mathcal{P}_l = (\mathbf{p}_r^0, \mathbf{p}_r^1, ..., \mathbf{p}_r^l)$. Consider a discretized spatial domain where the region of interest is partitioned into equal grid cells, and denote \mathcal{X} as the complete set of all discretized grid cells. The goal of this paper is to recover the true trajectory \mathcal{P}_l and build a radio map model $\mathcal{M} = \{(\mathbf{p}_r, \mathbf{g}_r) : \mathbf{p}_r \in \mathcal{X}\}$ that captures the full CSI vectors for all N_b BSs at UE locations \mathbf{p}_r , using only $\{\mathring{\mathcal{G}}_l\}$ without access to the corresponding location labels $\{\mathcal{P}_l\}$.

B. Coarse Location Recovery

Based on the sparse CSI observation \mathring{g}_{r}^{l} at time slot l, we first obtain a coarse estimate $\overline{\mathbf{p}}_{r}^{l}$ on the UE location, using some existing localization algorithms available in the literature, such as weighted centroid localization [27], as the BS locations are known. Note that the localization error of $\overline{\mathbf{p}}_{r}^{l}$ can be quite large, e.g., can be up to 100 meters, as the UE can probably locate in the NLOS region of some BSs, and therefore, $\overline{\mathbf{p}}_{r}^{l}$ cannot be directly used for radio map construction. In the rest of the paper, we simply assume the availability of the coarse location estimate $\overline{\mathbf{p}}_{r}^{l}$.

C. Joint Trajectory Recovery and Radio Map Construction

Let $\bar{\mathcal{P}}_L$ be the sequence of coarse location estimates $\bar{\mathbf{p}}_r^l$ collected along the trajectory. Denote $p(\mathcal{G}_L,\mathcal{P}_L;\mathcal{M}|\mathring{\mathcal{G}}_l)$ as the joint distribution of UE locations and their associated CSI conditioned on the sparse CSI measurements $\mathring{\mathcal{G}}_l$. A maximum log-likelihood problem for joint trajectory recovery and radio map construction is formulated as

$$\begin{array}{ll} \underset{\mathcal{G}_{L},\mathcal{P}_{L}}{\text{maximize}} & \log p(\mathcal{G}_{L},\mathcal{P}_{L};\mathcal{M}|\mathring{\mathcal{G}}_{l}) + \lambda \Gamma(\mathcal{P}_{L},\bar{\mathcal{P}}_{L}) \\ \text{subject to} & \mathbf{p}_{\mathrm{r}}^{l} \in \mathcal{X}, \quad l = 0, 1, ...L. \end{array} \tag{3}$$

where $\Gamma(\mathbf{p}_{\mathrm{r}}^{l}, \bar{\mathbf{p}}_{\mathrm{r}}^{l})$ is a value function to regularize the location variable \mathcal{P}_{L} to the coarse estimates $\bar{\mathcal{P}}_{L}$, and λ is a regularization parameter.

The joint optimization of trajectory recovery and radio map construction in (3) is challenged due to their mutual dependency. Recovering the trajectory \mathcal{P}_L requires the prior knowledge of radio map \mathcal{M} , while radio map \mathcal{M} construction

itself depends on correctly aligned pairs of \mathcal{P}_L and \mathcal{G}_L . To solve this coupled problem, we propose a deep learning solution by modeling complex spatial-temporal correlations between trajectories and channels, which enables efficient end-to-end optimization through gradient-based learning.

III. A GENERATIVE ARCHITECTURE FOR TRAJECTORY RECOVERY AND RADIO MAP CONSTRUCTION

In this section, we propose a deep generative architecture to solve the optimization problem in (3). We formulate the joint distribution $p(\mathcal{G}_L, \mathcal{P}_L; \mathcal{M}|\mathring{\mathcal{G}}_l)$ using an RNN based probabilistic model, and develop a specialized variational autoencoder (VAE) based generative framework to address the problem.

According to Bayes' theorem, the joint probability $p(\mathcal{G}_L, \mathcal{P}_L; \mathcal{M}|\mathring{\mathcal{G}}_l)$ can be factorized as

$$p(\mathcal{G}_{L}, \mathcal{P}_{L}; \mathcal{M} | \mathring{\mathcal{G}}_{l}) = \prod_{l=1}^{L} p(\mathbf{p}_{r}^{l} | \mathbf{p}_{r}^{0:l-1}, \mathring{\mathcal{G}}_{l}; \mathcal{M})$$

$$\times p(\mathbf{p}_{r}^{0} | \mathring{\boldsymbol{g}}_{r}^{0}; \mathcal{M}) \prod_{l=0}^{L} p(\boldsymbol{g}_{r}^{l} | \mathbf{p}_{r}^{l}; \mathcal{M})$$
(4)

where $\mathbf{p}_{\mathbf{r}}^{x:y}$ denotes the sequence of UE positions from time slot x to y. To model the temporal motion dynamics, we introduce a latent state \mathbf{S}^l that encodes all historical motion information up to time l-1. The state evolves recursively as

$$S^{l} = f_{\theta}(\mathbf{p}_{r}^{l-1}, \mathring{\mathbf{g}}_{r}^{l-1}, S^{l-1})$$
 (5)

where $f_{\theta}(\cdot)$ denotes the transition function parameterized by θ . By leveraging the hidden state S^l , the joint probability $p(\mathcal{G}_T, \mathcal{P}_T; \mathcal{M}|\mathring{\mathcal{G}}_l)$ is reformulated in a recurrent form as

$$p(\mathcal{G}_{L}, \mathcal{P}_{L}; \mathcal{M} | \mathring{\mathcal{G}}_{l}) = p(\mathbf{p}_{r}^{0} | \mathring{\boldsymbol{g}}_{r}^{0}; \mathcal{M}) \prod_{l=1}^{L} p(\mathbf{p}_{r}^{l} | \boldsymbol{S}^{l}, \mathring{\boldsymbol{g}}_{r}^{l}; \mathcal{M})$$

$$\times \prod_{l=0}^{L} p(\boldsymbol{g}_{r}^{l} | \mathbf{p}_{r}^{l}; \mathcal{M}).$$
(6)

Based on this factorization, the optimization problem in (3) can be reformulated as

$$\max_{\mathcal{G}_{L}, \mathcal{P}_{L}} \sum_{l=1}^{L} \log p(\mathbf{p}_{r}^{l} | \mathbf{S}^{l}, \mathring{\mathbf{g}}_{r}^{l}; \mathcal{M}) + \log p(\mathbf{p}_{r}^{0} | \mathring{\mathbf{g}}_{r}^{0}; \mathcal{M}) \\
+ \sum_{l=0}^{L} \log p(\mathbf{g}_{r}^{l} | \mathbf{p}_{r}^{l}; \mathcal{M}) + \lambda \Gamma(\mathcal{P}_{L}, \bar{\mathcal{P}}_{L}) \\
\text{subject to} \quad \mathbf{p}_{r}^{l} \in \mathcal{X}, \quad l = 0, 1, ...L.$$
(7)

We parameterize the optimization problem (7) as the objective of a VAE based generative framework, where the first two term corresponds to the encoder that maps the CSI \mathring{g}_{r}^{l} into a latent representation \mathbf{p}_{r}^{l} , the conditional likelihood $p(\mathbf{g}_{r}^{l}|\mathbf{p}_{r}^{l};\mathcal{M})$ serves as the decoder to reconstruct the CSI from the latent space, and the prior knowledge over the latent space is captured by a radio map \mathcal{M} . However, we still need to address the following technical challenges:

 Directly feeding sparse CSI data into the encoder is ineffective, as critical channel features are often lost or

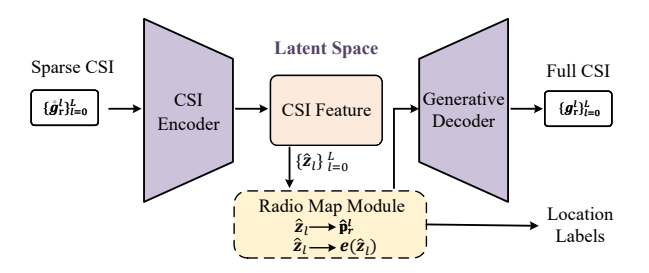


Figure 1. Diagram of a radio-map-embedded generative architecture.

obscured. A robust feature extraction module is essential to enhance CSI representation before encoding.

- Embedding radio map M into the network is a critical challenge. Parameterizing M as a latent variable may be inefficient, as its dimensionality explodes with map resolution and antenna numbers. More fundamentally, the absence of a latent prior precludes the Kullback-Leibler (KL) regularizer essential for stable VAE training, while the discrete structure of the radio map makes direct gradient-based optimization intractable.
- The self-supervised objective in (7) cannot guarantee that
 the learned latent space aligns with physical locations.
 Without explicit regularization, the network is free to
 learn representations that can be geometrically inconsistent with the physical space.

To address these challenges, we propose a radio-mapembedded generative architecture. A hybrid RNN encoder equipped with dual-scale feature extraction is designed to learn the mobility dynamics $p(\mathbf{p}_{\mathrm{r}}^{l}|\mathbf{S}^{l},\mathring{\mathbf{g}}_{\mathrm{r}}^{l};\mathcal{M})$ from sparse inputs. Instead of directly embedding the raw CSI map, we propose to learn a compact radio map embedding that encodes highlevel positional features, and implement the generative decoder $p(\mathbf{g}_{l}|\mathbf{p}_{\mathrm{r}}^{l};\mathcal{M})$ via a diffusion model. We further formulate a composite loss function that integrates multiple objectives to ensure temporal coherence of trajectory recovery. The rest of the paper focuses on designing the encoder, the radio map module, the decoder, and the loss function for training.

A. Radio-Map-Embedded Generative Architecture

A radio-map-embedded generative architecture for problem (7) is shown in Fig. 1. The overall architecture is consisted of a CSI encoder, a radio map module and a generative decoder.

The CSI encoder is designed to exploit both temporal dynamics and spatial correlations from the sequence of sparse CSI measurements, and effectively distill the incomplete CSI data into a compact latent representation that preserves the intrinsic mobility patterns for trajectory prediction.

The radio map module acts as the core latent prior to bridge the gap between the latent representation of CSI features and positional features. This module integrates a learnable radio map \mathcal{M} and a location predictor, where the radio map captures the CSI statistics of the environment, and the predictor infers location estimates from the CSI features. Unlike conventional Gaussian priors or black-box mappings, the radio map \mathcal{M} explicitly captures the intrinsic correspondence between CSI and spatial locations, which can align the latent space with the

physical environment for location recovery. It also serves as a rich repository of channel statistics to provide informative prior knowledge that supports high-fidelity CSI reconstruction.

Finally, a generative decoder reconstructs the full CSI by leveraging prior knowledge from the radio map \mathcal{M} . By using such statistical priors as guidance, the generative decoder can reconstruct higher-fidelity CSI, while rendering the generative process both controllable and interpretable.

B. Hybrid RNN-CNN based CSI Encoder

The CSI encoder architecture for joint trajectory recovery and radio map learning is shown in Fig. 2. The module consists of a CSI feature extractor to handle sparse inputs and a hybrid RNN-CNN encoder to learn mobility patterns.

1) CSI Feature Extractor: Highly sparse CSI inputs introduce substantial prediction uncertainty, as missing channel information can create an ill-posed mapping where a single sparse CSI corresponds to multiple possible locations. This ambiguity propagates through the encoder and degrades long-term tracking performance. Therefore, a CSI feature extractor is designed to enhance feature representation at two scales.

On one hand, strong angular correlations exist among beams, as neighboring beams often share angular coverage and capture similar propagation paths. Motivated by this, we adopt a self-attention module as our primary feature extractor to globally model angular dependencies across angular space and infer missing beam features from highly correlated beams.

On the other hand, CSI samples from nearby locations exhibit stronger spatial correlation, as large-scale channel characteristics vary smoothly across local areas. To exploit this, we apply multi-scale convolutions on neighboring CSI samples to capture spatial correlations at different granularities.

As shown in Fig. 2, the module features a hybrid architecture of two stacked attention-convolutional blocks. Each block integrates a Transformer structure with multi-head attention to capture beam-space dependencies, followed by double multi-scale convolutions and feedforward layers to extract local spatial correlations. A fully connected network (FCN) then maps the features into a compact latent representation.

Let $\{\hat{\boldsymbol{g}}_{\mathrm{r}}^{l}, \boldsymbol{m}^{l}\}_{l=0}^{L}$ be the input sequence of sparse CSI samples. At each time step l, the initial CSI feature vector $\boldsymbol{z}_{l}^{(0)}$ is extracted via a Transformer block as

$$\boldsymbol{z}_{l}^{(0)} = f_{trans}([\mathring{\boldsymbol{g}}_{r}^{l}, \boldsymbol{m}_{l}]) \tag{8}$$

where $f_{trans}(\cdot)$ represents the Transformer block, and $[\cdot,\cdot]$ denotes column-wise concatenation.

The output of the attention-convolutional block at time step l is thus implemented by

$$\boldsymbol{z}_{l}^{(1)} = f_{n1}([f_{c1}(\operatorname{stack}(\boldsymbol{z}_{l-k:l}^{(0)})), f_{c2}(\operatorname{stack}(\boldsymbol{z}_{l:l+k}^{(0)}))])$$
(9)

where $f_{c1}(\cdot)$ and $f_{c2}(\cdot)$ represent multi-scale convolutional layers applied to the spatial neighborhoods before and after the current position, respectively, and $f_{n1}(\cdot)$ is a feedforward layer that fuses dual-context features. The function $\operatorname{stack}(\cdot)$ represents row-wise concatenation across multiple vectors, and k defines the size of convolutional windows.

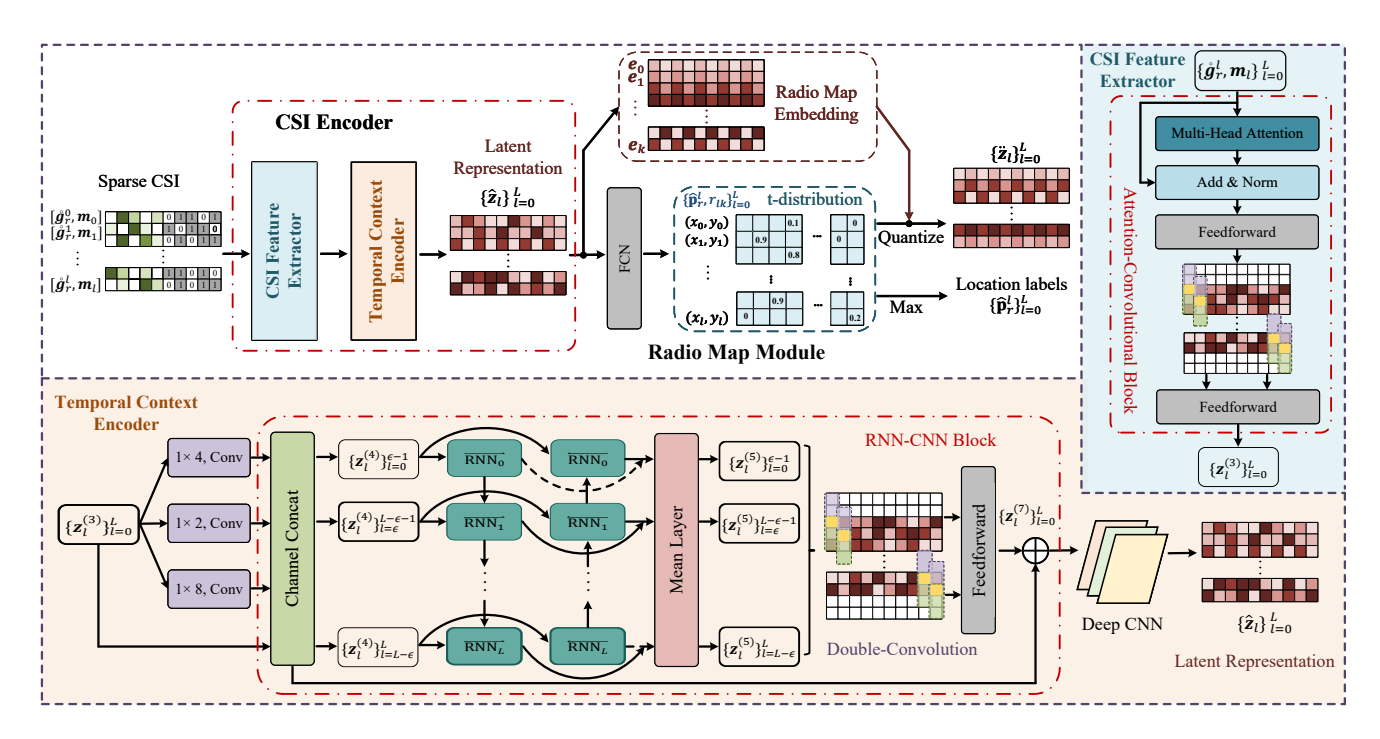


Figure 2. The proposed hybrid RNN-CNN based CSI encoder for joint trajectory recovery and radio map learning.

Let $\mathbf{z}_l^{(2)}$ be the output of the second attention-convolutional block. The final feature representation is then obtained as $\mathbf{z}_l^{(3)} = f_{NN1}(\mathbf{z}_l^{(2)})$, where $f_{NN1}(\cdot)$ represents the mapping performed by the FCN.

2) Temporal Context Encoder: The wireless channel exhibits short-term temporal correlation, where CSI samples close in time are highly correlated. Since recent observations provide the most informative cues for the current position and channel state, we adopt an RNN-based design to learn implicit motion dynamics from the extracted CSI features.

However, a convolutional RNN inherently relies solely on past information and is prone to error accumulation over time. This becomes particularly critical when historical observations are scarce, as the initial hidden state often suffers from a large bias due to insufficient temporal context, which can degrade early-stage predictions and slow down convergence.

To address this issue, we introduce a hybrid RNN-CNN based encoder architecture with two key enhancements:

- Bidirectional Inference with Truncation: We adopt a bidirectional RNN to leverage future observations as complementary context, while a truncation strategy discards highly biased initial hidden states to mitigate the impact of early high-error predictions.
- CNN-based State Refinement: To address error accumulation and state drift, a multi-scale CNN module refines the RNN hidden states through local temporal aggregation, smoothing short-term fluctuations to improve robustness.

Therefore, the encoder consists of three hybrid RNN-CNN blocks with progressively increasing dimensionality to hierarchically extract temporal features, where each block sequentially fuses a bidirectional RNN for temporal context with double multi-scale convolutions for local refinement. The resulting hierarchical features are then processed by a deep

CNN and a feedforward layer to reduce dimensionality and generate the representation of positional deatures. The details are illustrated as follows.

At time step l, the input feature $z_l^{(3)}$ is first processed by a lightweight CNN with parallel convolutions of varying kernels and strides to extract multi-scale features. These feature maps are subsequently concatenated as

$$\boldsymbol{z}_{l}^{(4)} = [\boldsymbol{z}_{l}^{(3)}, f_{c3}(\boldsymbol{z}_{l}^{(3)}), f_{c4}(\boldsymbol{z}_{l}^{(3)}), f_{c5}(\boldsymbol{z}_{l}^{(3)})] \tag{10}$$

where $f_{c3}(\cdot)$, $f_{c4}(\cdot)$ and $f_{c5}(\cdot)$ are convolutional layers.

For the hybrid RNN-CNN block, the feature sequence $\{\boldsymbol{z}_{l}^{(4)}\}_{l=0}^{L}$ is first fed into a bidirectional RNN, and the output sequence $\{\boldsymbol{z}_{l}^{(5)}\}_{l=0}^{L}$ is implemented as

$$\begin{aligned}
&\{\boldsymbol{z}_{l}^{(5)}\}_{l=0}^{\epsilon-1} = \{\operatorname{flip}(f_{r2}(\operatorname{flip}(\{\boldsymbol{z}_{l}^{(4)}\}_{l=0}^{L})))\}_{l=0}^{\epsilon-1} \\
&\{\boldsymbol{z}_{l}^{(5)}\}_{l=\epsilon}^{L-\epsilon-1} = (\operatorname{flip}(f_{r2}(\operatorname{flip}(\{\boldsymbol{z}_{l}^{(4)}\}_{l=0}^{L-\epsilon}))))\}_{l=\epsilon}^{L-\epsilon-1} \\
&\quad + \{f_{r1}(\{\boldsymbol{z}_{l}^{(4)}\}_{l=0}^{L-\epsilon})\}_{l=\epsilon}^{L-\epsilon})/2
\end{aligned} \tag{11}$$

$$\{\boldsymbol{z}_{l}^{(5)}\}_{l=L-\epsilon}^{L} = \{f_{r1}(\{\boldsymbol{z}_{l}^{(4)}\}_{l=0}^{L})\}_{l=L-\epsilon}^{L}$$

where $f_{r1}(\cdot)$, $f_{r2}(\cdot)$ are the forward and backward RNNs, flip(·) denotes temporal reversal, and ϵ is the truncation length.

Following the RNN, the feature sequence $\{z_l^{(5)}\}_{l=0}^L$ are processed by double multi-scale convolutional layers for local refinement across multiple time steps, which is formulated as

$$\mathbf{z}_{l}^{(6)} = f_{n2}([f_{c6}(\operatorname{stack}(\mathbf{z}_{l-k:l}^{(5)})), f_{c7}(\operatorname{stack}(\mathbf{z}_{l:l+k}^{(5)}))])$$
 (12)

where $f_{c6}(\cdot)$, $f_{c7}(\cdot)$ are convolutional layers, and $f_{n2}(\cdot)$ is a feedforward layer to fuse the dual-context features.

The feature sequence $\{z_l^{(6)}\}_{l=0}^L$ are further refined by two stacked hybrid RNN-CNN blocks to progressively enhance temporal feature representations. Let $\{z_l^{(7)}\}_{l=0}^L$ be the output features from the final RNN-CNN block. In the final stage,

the refined feature $z_l^{(7)}$ is passed through a deep CNN to extract spatially-aware latent representations that encode the underlying positional features, which is expressed as

$$\hat{\boldsymbol{z}}_l = f_{n3}(\text{flatten}(f_{cnn}(\text{reshape}(\boldsymbol{z}_l^{(7)}))))$$
 (13)

where $f_{cnn}(\cdot)$ denotes the deep CNN, and $f_{n3}(\cdot)$ is a feedforward layer that generates the final latent representation. Here, reshape(\cdot) transforms the 1D feature vector into a 2D spatial feature map that is compatible with CNN, while flatten(\cdot) converts the CNN output back into a 1D feature vector.

C. Radio Map Module

We leverage a radio map to capture CSI knowledge in the latent space and align CSI features with physical location labels. Instead of directly embedding the raw CSI map, we propose to learn a compact radio map embedding $\mathcal E$ to reduce feature complexity, where each embedding vector corresponds to a physical location and encodes high-level positional features. A location predictor further maps the CSI features to a probabilistic distribution over possible locations.

- 1) Location Predictor: This module employs a FCN to transform the CSI features \hat{z}_l into physical location coordinates, which is designed for two purposes:
 - Physics-Informed Regularization: This module enables direct incorporation of physics-informed constraints into the training objective, such as the regularization term $\lambda \Gamma(\mathcal{P}_L, \bar{\mathcal{P}}_L)$ in (7). The resulting gradients are backpropagated to align the latent space with the physical space.
 - Latent Structuring via Positional Clustering: Since the
 first two terms in (7) lack a KL-based latent prior, we
 introduce a positional clustering loss in the physical coordinate space. By encouraging predicted locations to form
 spatially meaningful clusters consistent with observed
 mobility or geographic constraints, the latent space is
 implicitly guided toward a structured, data-driven prior.

Consequently, the location at time step l is obtained by

$$\hat{\mathbf{p}}_{\mathrm{r}}^{l} = f_{NN2}(\hat{\boldsymbol{z}}_{l}) \tag{14}$$

where $f_{NN2}(\cdot)$ represents the FCN mapping.

We further compute a soft assignment probability over grid cells using a Student's t-distribution. Denote $\{x_k\}_{k=1}^K \in \mathcal{X}$ as the locations of the grid cell centers. The probability that the predicted location belongs to the kth grid cell is given by

$$r_{lk} = \frac{(1 + ||\hat{\mathbf{p}}_{r}^{l} - \mathbf{x}_{k}||^{2}/\alpha)^{-\frac{\alpha+1}{2}}}{\sum_{k'}^{K} (1 + ||\hat{\mathbf{p}}_{r}^{l} - \mathbf{x}_{k'}||^{2}/\alpha)^{-\frac{\alpha+1}{2}}}$$
(15)

where α denotes the degree of freedom of the Student's t-distribution. This soft assignment provides a probabilistic location estimate over the discrete grid, which is subsequently used in the positional clustering loss to guide the latent space toward a more structured and geographically-aware representation.

2) Radio Map Quantization: This module discretizes the continuous latent representations by mapping each vector to its nearest neighbor in the radio map embedding \mathcal{E} . By quantizing the continuous space into a finite set of discrete codes, the model is encouraged to learn a structured, compact

representation aligned with the intrinsic properties of radio maps. This discretization also clusters similar inputs under the same code, enabling the radio map to capture high-level categorical features corresponding to distinct spatial regions.

Define a radio map embedding $\mathcal{E} \in \mathbb{R}^{K \times D}$, where K denotes the number of discrete latent categories (i.e., the number of grid cells in \mathcal{X}), and D is the dimensionality of each embedding vector $\mathbf{e}_k \in \mathbb{R}^D$ for k = 1, 2, ..., K, which matches the dimensionality of the feature $\hat{\mathbf{z}}_l$. The posterior categorical distribution $q(\hat{\mathbf{z}}_l = k|\mathbf{g}_l)$ is defined as a one-hot distribution, which is formulated as

$$q(\hat{\boldsymbol{z}}_l = k | \hat{\boldsymbol{g}}_{\mathbf{r}}^l) = \begin{cases} 1 & \text{for } k = \operatorname{argmin}_k || \hat{\boldsymbol{z}}_l - \boldsymbol{e}_k || \\ 0 & \text{otherwise} \end{cases}$$
(16)

Rather than quantizing the feature space directly, we obtain the discrete representation \ddot{z}_l by passing \hat{z}_l through a discretization bottleneck and mapping it to the nearest embedding vector based on physical proximity:

$$\ddot{z}_l = e_k$$
, where $k = \operatorname{argmax}_k |r_{lk}|$. (17)

Mapping in the physical coordinate space explicitly aligns latent features with actual locations, with nearby points assigned to similar embedding vectors to maintain physically consistency in the latent space.

D. Diffusion-Based Generative Decoder

The generative decoder is illustrated in Fig. 3. We adopt a conditional denoising diffusion probabilistic model (DDPM) that takes \ddot{z}_l as the guidance prompt to reconstruct the full CSI. Unlike deterministic mapping, DDPM can capture the inherent uncertainty and spatial variability of CSI, and learn a probabilistic mapping that reflects the stochastic nature of real wireless channels. The representation \ddot{z}_l encodes positional and CSI statistical features, guiding the model to generate controllable, physically consistent CSI that aligns with the channel characteristics captured by the radio map.

The generative decoder is implemented using a conditional DDPM that consists of a forward diffusion process and a reverse denoising process, where the representation \ddot{z}_l provides contextual prompt to effectively guide the denoising process.

1) Forward Diffusion Process: The forward process is formulated as a Markov chain that incrementally adds Gaussian noise over T step. The state transition at each step of the forward diffusion process is defined as

$$q(\boldsymbol{g}_{\mathrm{r}}^{l,(t)}|\boldsymbol{g}_{\mathrm{r}}^{l,(t-1)}) = \mathcal{N}(\sqrt{1-\eta_{t}}\boldsymbol{g}_{\mathrm{r}}^{l,(t-1)},\eta_{t}\boldsymbol{I})$$
(18)

where η_t denotes the variance schedule parameter at step t, which gradually increases with t. According to the property of Gaussian distribution, the noisy sampls $g_{\rm r}^{l,(t)}$ at an arbitrary timestep t can be directly computed from the clean sample $g_{\rm r}^{l,(0)}$ (i.e., $g_{\rm r}^l$ without any noise), which is given by

$$q(\boldsymbol{g}_{\mathrm{r}}^{l,(t)}|\boldsymbol{g}_{\mathrm{r}}^{l,(0)}) = \mathcal{N}(\sqrt{\bar{\alpha}_{t}}\boldsymbol{g}_{\mathrm{r}}^{l,(0)}, (1 - \bar{\alpha}_{t})\boldsymbol{I})$$
(19)

where $\alpha_t = 1 - \eta_t$ and $\bar{\alpha} = \prod_{i=1}^t \alpha_i$. As a result, the noisy sample $g_r^{l,(t)}$ at any arbitrary time step t can be sampled as

$$\mathbf{g}_{\mathrm{r}}^{l,(t)} = \sqrt{\bar{\alpha}_t} \mathbf{g}_{\mathrm{r}}^{l,(0)} + \sqrt{1 - \bar{\alpha}_t} \boldsymbol{\varepsilon}$$
 (20)

where $\boldsymbol{\varepsilon} \sim \mathcal{N}(0, \boldsymbol{I})$ represents standard Gaussian noise.

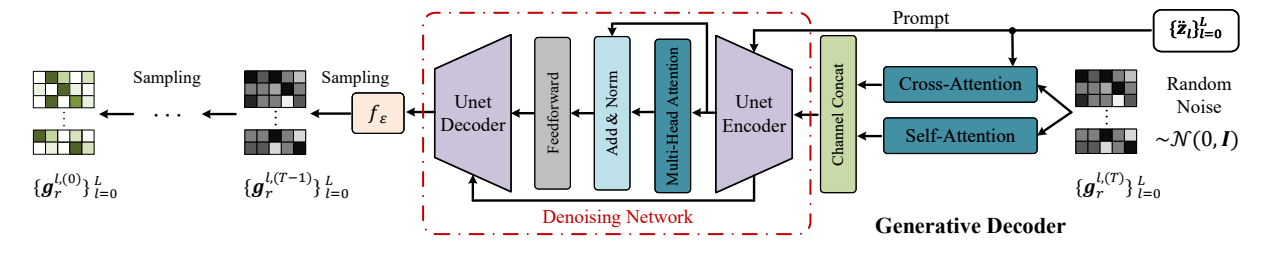


Figure 3. The proposed generative decoder conditioned on the radio map for full CSI reconstruction.

2) Reverse Denoising Process: The reverse denoising process progressively recovers the clean sample $\boldsymbol{g}_{\mathrm{r}}^{l,(0)}$ from the pure Gaussian noise $\boldsymbol{g}_{\mathrm{r}}^{l,(T)} \sim \mathcal{N}(0,\boldsymbol{I})$. Each reverse state transition conditioned on $\boldsymbol{g}_{\mathrm{r}}^{l,(0)}$ can be given by

$$q(\boldsymbol{g}_{\mathrm{r}}^{l,(t-1)}|\boldsymbol{g}_{\mathrm{r}}^{l,(t)},\boldsymbol{g}_{\mathrm{r}}^{l,(0)}) = \mathcal{N}(\frac{1}{\sqrt{\alpha_{t}}}(\boldsymbol{g}_{\mathrm{r}}^{l,(t)} - \frac{\eta_{t}}{\sqrt{1 - \bar{\alpha}_{t}}}) \times \varepsilon_{t}(\boldsymbol{g}_{\mathrm{r}}^{l,(0)})), \frac{1 - \bar{\alpha}_{t-1}}{1 - \bar{\alpha}_{t}} \eta_{t}\boldsymbol{I})$$
(21)

where $\varepsilon_t(\boldsymbol{g}_{\mathrm{r}}^{l,(0)}) = (\boldsymbol{g}_{\mathrm{r}}^{l,(t)} - \sqrt{\bar{\alpha}_t}\boldsymbol{g}_{\mathrm{r}}^{l,(0)})/\sqrt{1-\bar{\alpha}_t}$ denotes the noise at step t of the forward process which is related to $\boldsymbol{g}_{\mathrm{r}}^{l,(0)}$. However, $\boldsymbol{g}_{\mathrm{r}}^{l,(0)}$ is inherently unknown during the reverse

However, $g_{\rm r}^{l,(0)}$ is inherently unknown during the reverse process. To address this, a neural network is trained to predict the noise term $\varepsilon_t(g_{\rm r}^{l,(0)})$. Notably, the radio-map representation \ddot{z}_l is a feature mapping of $g_{\rm r}^{l,(0)}$, and captures its positional information and CSI statistics. As such, \ddot{z}_l inherently encodes informative cues that are highly correlated with $g_{\rm r}^{l,(0)}$. Based on this property, we propose using \ddot{z}_l as a conditioning prompt to guide the prediction of $\varepsilon_t(g_{\rm r}^{l,(0)})$.

We adopt an attention-augmented UNet to predict $\varepsilon_t(g_r^{l,(0)})$ as shown in Fig. 3. The input first passes through self-attention and cross-attention layers, where self-attention captures intrafeature dependencies and cross-attention integrates the conditional prompts. The encoder then compresses the feature maps into compact representations, followed by a bottleneck with additional attention to refine contextual features. The decoder subsequently restores spatial resolution via upsampling, assisted by skip connections that preserve fine-grained details.

Based on this denoising network, the predicted sample $\hat{g}_r^{l,(t-1)}$ from step t in the reverse process is generated by

$$\hat{\boldsymbol{g}}_{\mathrm{r}}^{l,(t-1)} = \frac{1}{\sqrt{\alpha_{t}}} (\hat{\boldsymbol{g}}_{\mathrm{r}}^{l,(t)} - \frac{\eta_{t}}{\sqrt{1 - \bar{\alpha}_{t}}} f_{\varepsilon}(\hat{\boldsymbol{g}}_{\mathrm{r}}^{l,(t)}, \ddot{z}_{l}, t)) + \sqrt{\frac{1 - \bar{\alpha}_{t-1}}{1 - \bar{\alpha}_{t}}} \eta_{t} \varepsilon.$$
(22)

where $f_{\varepsilon}(\cdot)$ denotes the proposed denoising network.

E. Training Objective

We design a composite training objective that incorporates reconstruction loss, physics-informed constraints, and tailored regularization terms to optimize the proposed model for joint trajectory recover and radio map construction.

1) Clustering Loss: We first extract coarse locations from the imprecise trajectory $\{\bar{\mathbf{p}}_{\mathrm{r}}^l\}_{l=1}^L$, and iteratively refine the clustering through a self-reinforcing auxiliary target distribution that emphasizes high-confidence assignments. A triplet

loss is further employed to improve cluster separability by drawing spatially similar points closer in the latent space and pushing dissimilar ones apart.

The coarse location information is initially extracted from the imprecise trajectory $\{\bar{\mathbf{p}}_{\mathrm{r}}^l\}_{l=1}^L$ through a loss function as

$$\mathcal{L}_c = ||\hat{\mathbf{p}}_r^l - \bar{\mathbf{p}}_r^l||. \tag{23}$$

We construct an auxiliary target distribution that emphasizes high-confidence cluster assignments. It is achieved by squaring the soft assignments r_{lk} to amplify confident predictions, while normalizing across samples to reduce the impact of imbalanced cluster sizes. The target distribution is defined as

$$p_{lk} = \frac{r_{lk}^2 / \sum_{l} r_{lk}}{\sum_{k'} r_{lk'}^2 / \sum_{l} r_{lk'}}.$$
 (24)

The model is trained to align the soft assignments with this refined self-reinforcing target distribution by minimizing their KL divergence, which is implemented by

$$\mathcal{L}_s = \sum_{l} \sum_{k} p_{lk} \log \frac{p_{lk}}{r_{lk}}.$$
 (25)

To further preserve the physical spatial structure, we incorporate a triplet loss that pulls samples with similar local geometry closer while pushing dissimilar ones apart. We define a set of triplets from the set of sample indices L as

$$\mathcal{T} = \{ (n, c, f) \in L^3 : 0 < |t_n - t_c| \le T_c < |t_n - t_f| \}$$
 (26)

where t_n , t_c , and t_f denote the timestamps of the anchor, positive, and negative samples, respectively, and $T_c>0$ is a coherence-time threshold that determines temporal closeness. Intuitively, if t_n is closer to t_c than to t_f , the spatial distance $||\hat{\mathbf{p}}_{\rm r}^n - \hat{\mathbf{p}}_{\rm r}^c||$ is expected to be smaller than $||\hat{\mathbf{p}}_{\rm r}^n - \hat{\mathbf{p}}_{\rm r}^f||$. Accordingly, the triplet loss is formulated as

$$\mathcal{L}_t = \frac{1}{|\mathcal{T}|} \sum_{(n,c,f)\in\mathcal{T}} \max(||\hat{\mathbf{p}}_r^n - \hat{\mathbf{p}}_r^c|| - ||\hat{\mathbf{p}}_r^n - \hat{\mathbf{p}}_r^f|| + Q_t, 0)$$
(27)

where Q_t is the margin parameter that enforces $\hat{\mathbf{p}}_r^n$ to be at least Q_t closer to $\hat{\mathbf{p}}_r^c$ than to $\hat{\mathbf{p}}_r^f$.

2) Physical Dynamics Loss: Due to inertia and mechanical constraints, real-world object motion tends to exhibit smooth acceleration patterns. Therefore, physically plausible trajectories are expected to be continuous and temporally coherent.

To incorporate this physical prior, we introduce a physical dynamics loss that enforces realistic motion by minimizing acceleration variations using the second-order differences of consecutive predicted positions, which is implemented by

$$\mathcal{L}_d = \frac{1}{L-2} \sum_{l=2} ||\hat{\mathbf{p}}_{r}^{l+1} - 2\hat{\mathbf{p}}_{r}^{l} + \hat{\mathbf{p}}_{r}^{l-1}||^2.$$
 (28)

By penalizing abrupt acceleration changes, this loss promotes smoother trajectories that follow physical motion dynamics.

3) Reconstruction Loss: The reconstruction loss supervises the training of the reverse denoising network $f_{\varepsilon}(\cdot)$ to generate high-quality CSI, and is formulated as

$$\mathcal{L}_r = \mathbb{E}_{\boldsymbol{g}_l, \boldsymbol{\varepsilon}, t}[||\boldsymbol{\varepsilon} - f_{\varepsilon}(\boldsymbol{g}_l^{(t)}, \ddot{\boldsymbol{z}}_l, t)||^2] + ||\operatorname{sg}(\hat{\boldsymbol{z}}_l) - \ddot{\boldsymbol{z}}_l||^2$$
(29)

where the first term represents the reconstruction loss, the second term is the commitment loss that encourages the encoder output \hat{z}_l close to the radio map embedding \ddot{z}_l , and $sg(\cdot)$ denotes the stop-gradient operator.

4) Model Training: We implement the proposed network in Pytorch and the Adam optimizer is utilized.

The encoder and decoder are jointly trained with a composite loss that integrates all objectives as

$$\mathcal{L}_{total} = \mathcal{L}_s + \mathcal{L}_r + \lambda_c \mathcal{L}_c + \lambda_t \mathcal{L}_t + \lambda_d \mathcal{L}_d \tag{30}$$

where λ_c , λ_e and λ_d are hyperparameters that balance the contribution of the auxiliary regularization terms.

For radio map learning, we adopt the exponential moving average (EMA) strategy [28] to update embedding vectors. Unlike gradient backpropagation that may suffer from gradient instability, EMA improves stability by updating each embedding vector as a smooth moving average of its encoder outputs, which help prevent gradient instability and mode collapse.

Specifically, for each radio map embedding vector e_k , let m_k be the accumulated sum of the encoder outputs \hat{z}_l assigned to e_k according to (17), and N_k be the number of times that this vector is selected. The update rules are given by

$$m_{k}^{(t)} = \gamma m_{k}^{(t-1)} + (1 - \gamma) \sum_{i \in \mathcal{I}_{k}} \hat{\boldsymbol{z}}_{l}^{(i)}$$

$$N_{k}^{(t)} = \gamma N_{k}^{(t-1)} + (1 - \gamma) |\mathcal{I}_{k}|$$

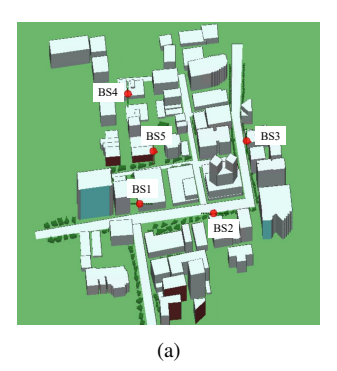
$$\boldsymbol{e}_{k}^{(t)} = \frac{m_{k}^{(t)}}{N_{k}^{(t)} + \zeta}$$
(31)

where γ is the decay factor, \mathcal{I}_k denotes the set of samples assigned to the vector e_k , $|\mathcal{I}_k|$ indicates the number of samples in \mathcal{I}_k , and ζ is a small constant to prevent division by zero.

IV. EXPERIMENT RESULTS

This section presents numerical results to demonstrate the effectiveness of the proposed model. Evaluations are conducted on two datasets: a simulated outdoor dataset generated by RT software *Wireless InSite* in realistic urban terrain, and an indoor dataset obtained from real-world measurements.

In the simulated scenario, the urban topology covers a $710~\text{m} \times 740~\text{m}$ area of San Francisco, USA, as shown in Fig. 4(a). Five BSs with 16-element MIMO antenna array are deployed on the selected rooftops, and a discrete Fourier transform (DFT) codebook is used. Mobile UEs at 2 m height follow random walk trajectories along roads. Channel data are generated with up to 6 reflections and 1 diffraction. A



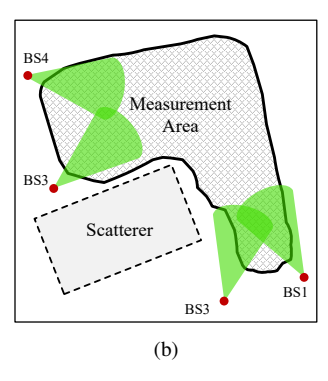


Figure 4. Environmental topology: a) Scenario I: 3D terrain of the outdoor urban environment; b) Scenario II: Top view of the indoor environment [29].

sinusoidal waveform at 2.8 GHz with 100 MHz bandwidth is used. In total, CSI measurements were collected at 18844 locations along the main routes, capturing rich propagation characteristics such as blockage and reflection, providing a comprehensive dataset for modeling and analysis.

In the indoor scenario, we utilize the DICHASUS dataset [29], which provides channel measurements from a distributed MIMO communication system in a factory environment. The top-view layout is plotted in Fig. 4(b). In this setup, the system includes four TXs, each equipped with a 2×4 uniform rectangular antenna array. Channels are measured at 1.272 GHz with 50 MHz bandwidth. A mobile robot with an RX moves along multiple trajectories within an L-shaped area, at an approximate height of 0.94 meter. In total, 16,778 position-labeled channel samples are recorded.

The following baselines are compared with the proposed model, which are summarized as:

- Radio-map-assisted SKF [26]: This work leverages radio maps as prior information and employs a Kalman filter to infer user trajectories from coarse location labels and jointly estimate the channel covariance.
- 2) Semi-supervised CC (e.g., [22, 23]): These self-supervised CC methods use only a small portion of true location labels for calibration. The loss function combines triplet loss and location supervision as $\mathcal{L}_{chart} = \lambda_t \mathcal{L}_t + \lambda_c \mathcal{L}_c$. We consider two variants:
 - Semi-CC-GT: Using noise-free ground-truth RX locations in \mathcal{L}_c for the ideal supervision scenario;
 - Semi-CC-Noisy: Using coarse and noisy RX location labels in \mathcal{L}_c to simulate location uncertainty.
- 3) Real-world CC [25]: This CC method uses only TX location labels, positioning the RX closer to the TX with stronger received signals, thereby leveraging TX locations as weak supervision in place of RX labels.
- 4) CAM-aided CSI tracking [30]: It employs $M=N_t/2$ beam vectors from the estimated AOD with the constructed channel angle map (CAM) for channel sensing, and uses the least squares method for CSI tracking.

The proposed model is evaluated using the following metrics: 1) Localization error: For true positions $\mathbf{p}_{\mathrm{r}}^{l}$ and estimates $\hat{\mathbf{p}}_{\mathrm{r}}^{l}$, the localization error is defined as $\frac{1}{L}\sum_{l}^{l}||\hat{\mathbf{p}}_{\mathrm{r}}^{l}-\mathbf{p}_{\mathrm{r}}^{l}||$. 2) 95th percentile: The value below which 95% of the Euclidean

distance errors fall. 3) Trustworthiness (TW): This metric measures how well the local structure in the latent space reflects that in the real-world space, which is given by

$$TW(k) = 1 - \gamma \sum_{l}^{L} \sum_{j \notin \mathcal{V}_{l}, j \in \hat{\mathcal{V}}_{l}} (d(l, j) - k)$$
 (32)

where \mathcal{V}_l and $\hat{\mathcal{V}}_l$ are the sets of the k nearest neighbors of point l in the real and latent spaces, $d(l,j) = ||\mathbf{p}_{\mathrm{r}}^l - \mathbf{p}_{\mathrm{r}}^j||$ is the distance between $\mathbf{p}_{\mathrm{r}}^l$ and $\mathbf{p}_{\mathrm{r}}^j$, and $\gamma = 2/(Lk(2L-3k-1))$ is a normalization factor. 4) Continuity (CT): This metric quantifies how well the neighborhood relationships in the realworld space are preserved in the latent space, defined as

$$CT(k) = 1 - \gamma \sum_{l}^{L} \sum_{j \in \mathcal{V}_{l}, j \notin \hat{\mathcal{V}}_{l}} (\hat{d}(l, j) - k)$$
(33)

where $\hat{d}(l,j) = ||\hat{\mathbf{p}}_{r}^{l} - \hat{\mathbf{p}}_{r}^{j}||$ denotes the distance between $\hat{\mathbf{p}}_{r}^{l}$ and $\hat{\mathbf{p}}_{r}^{j}$. 5) Root mean square error (RMSE) and normalized mean square error (NMSE): Measure the average reconstruction error between the normalized predicted radio map and the ground truth. 6) Channel capacity: It is given by $f(\mathbf{h}(\tilde{\mathbf{p}}), \mathbf{w}) = \log_{2}(1+P_{t}|\mathbf{h}(\tilde{\mathbf{p}})\mathbf{w}|^{2}/\sigma_{n}^{2})$ where \mathbf{w} is the beamforming vector, P_{t} is the transmitted power and σ_{n}^{2} denotes the noise variance.

A. Trajectory Recovery for Outdoor Scenario

In this experiment, we evaluate the trajectory recovery performance of the proposed model in the outdoor scenario. Both the proposed model and the radio-map-assisted SKF use a radio map with a 5 m grid resolution. The imprecise trajectory $\{\bar{\mathbf{p}}_r^l\}_{l=1}^L$ is obtained by adding Gaussian noise with variance $\sigma^2=400$ to the ground-truth positions $\{\mathbf{p}_r^l\}_{l=1}^L$. For the proposed model, we set $\lambda_c=0.01,\ \lambda_t=1$ and $\lambda_d=50$. Semi-CC-Noisy uses the same λ_c and λ_t for triplet loss and imprecise supervision loss, while Semi-CC-GT uses 500 ground-truth location labels with $\lambda_c=1$.

First, we consider a trajectory moving uniformly along the main road at 1 m/s, with CSI sampled from all BSs every 0.1 seconds. Fig. 5 shows the ground truth trajectory and the predicted trajectories of all compared methods. It is observed that the proposed method and SKF closely match the ground truth; however, the proposed method produces a continuous trajectory with better temporal and spatial coherence, while SKF yields only discrete points along the path. Semi-CC-GT aligns well with the true path but shows noticeable local disturbances, whereas Semi-CC-Noisy suffers from substantial global deviations. Real-world CC performs the worst, likely because relying only on BS positional information is insufficient to reconstruct the physical trajectory in complex outdoor environments with rich channel diversity. A detailed summary of the performance comparisons is presented in Table I. The proposed method outperforms all baselines across all metrics, reducing localization error by 32% over SKF and 28% over Semi-CC-GT. Among them, Semi-CC-GT performs comparably to the proposed method in TW and CT, with differences below 0.004. Although Real-world CC yields a large localization error, its TW and CT remain relatively high, indicating that the latent spatial structure is still well preserved.

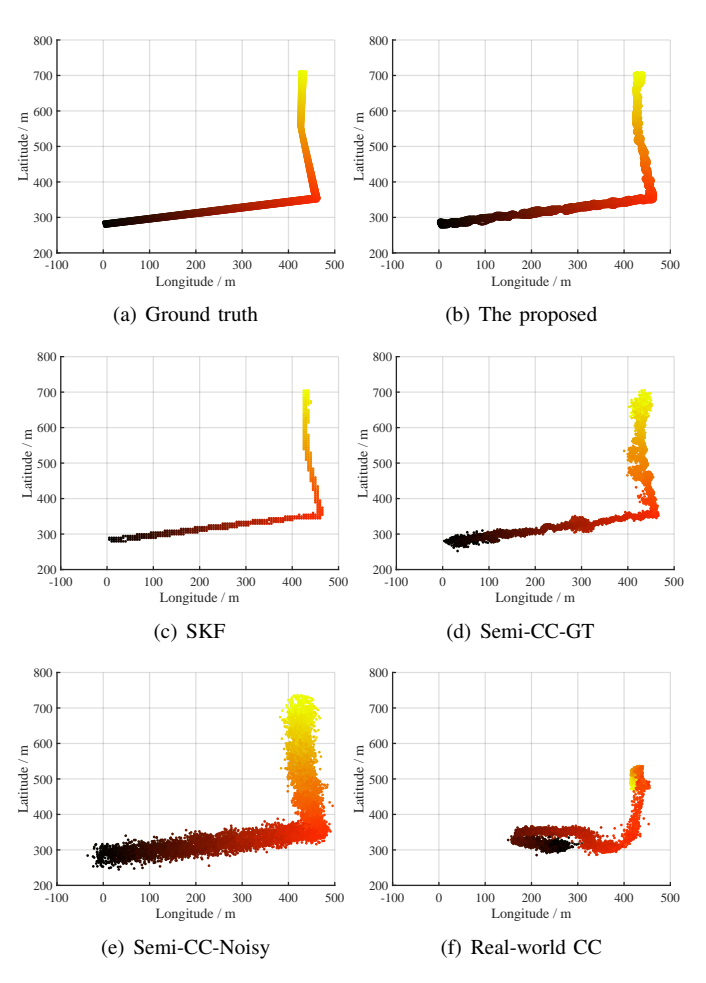


Figure 5. Trajectory recovery results for the outdoor scenario, where the UE moves continuously at 1 m/s along the main road in a back-and-forth pattern.

Table I
POSITIONING PERFORMANCE COMPARISON FOR OUTDOOR SCENARIO

	Latent Space Quality		Positioning Error / m	
Scheme	TW↑	CT ↑	Mean ↓	95th Percentile ↓
SKF	0.986	0.987	7.24	14.78
Semi-CC-GT	0.990	0.994	6.81	19.57
Semi-CC-Noisy	0.978	0.982	14.61	29.79
Real-world CC	0.963	0.965	82.75	217.41
Proposed	0.995	0.995	4.90	9.92

Second, we consider a more complex mobile trajectory with stops and speed variations. In this scenario, the UE moves at 1 m/s, and pauses for 30 seconds at a specific location. Additionally, the UE will accelerate from 1 m/s up to 10 m/s with an acceleration rate of 1 m/s², maintains this high speed for a period, and finally decelerates back to 1 m/s. Fig. 6 presents the recovery results for the complex trajectory. The stop position (blue star) corresponds to repeated samples at the same point, with small perturbations added for clearer visualization. It is observed that the proposed model effectively learns the acceleration behavior and partially

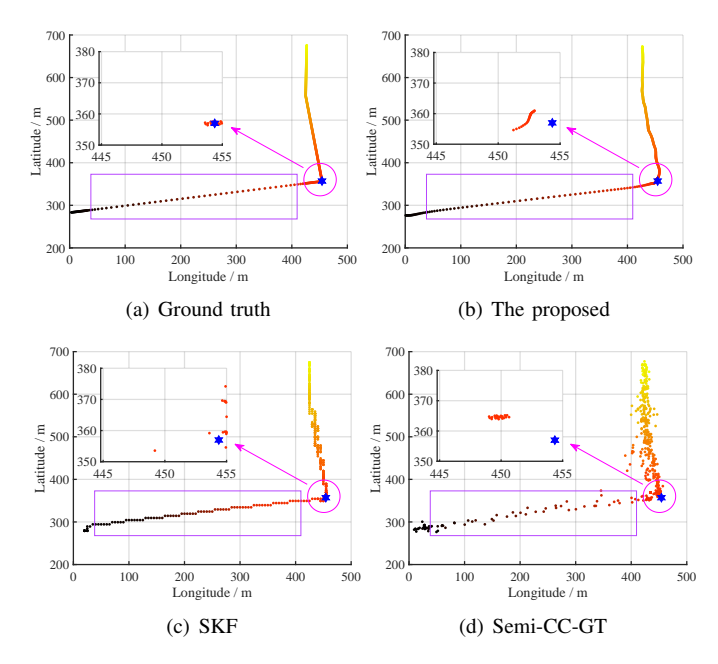


Figure 6. Trajectory recovery results under more complex motion dynamics. The blue star marks the stop location, while the purple segment indicates acceleration from 1 m/s to 10 m/s, followed by cruising and subsequent deceleration back to 1 m/s.

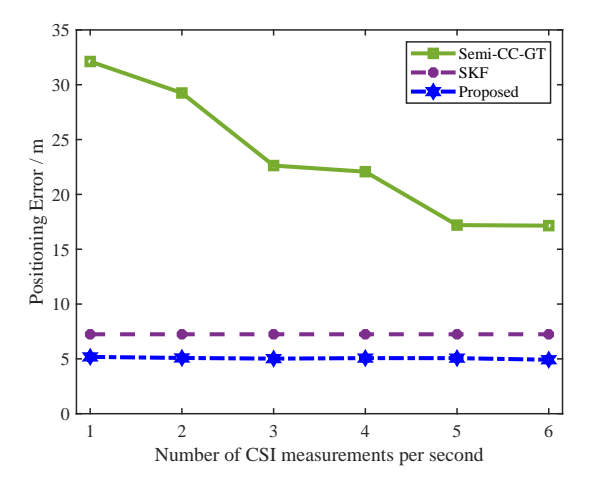


Figure 7. Positioning error versus the number of measurements M.

captures stationary segments. Semi-CC-GT, which is motion-independent, partially reflects both stationary and accelerated states, while SFM fails to model motion dynamics. Notably, the proposed method best aligns with the true trajectory during acceleration and successfully captures both the acceleration and deceleration phases. It also approximates stationary behavior by reducing the spacing between consecutive points while keeping them within the same grid cell, and preserves the transition from stationary to moving states.

We further evaluate trajectory recovery under varying numbers of CSI measurements M per second. Fig. 7 shows the positioning error versus the measurement number M. SKF shows no performance change as the measurement rate decreases. The proposed method exhibits only a minor degradation of about 0.2 meters even at M=1, which demonstrates strong robustness to sparse measurements. Across all settings, the

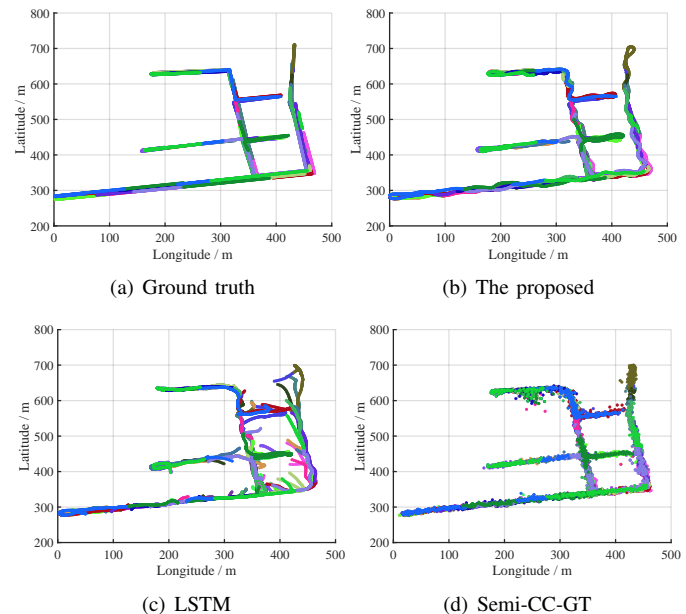


Figure 8. Generalization results across trajectories of varying lengths.

 ${\it Table \ II}$ Generalization Results for Trajectories of Arbitrary Lengths

	Latent Space Quality		Positioning Error / m	
Scheme	TW ↑	СТ ↑	Mean ↓	95th Percentile ↓
Semi-CC-GT	0.992	0.992	7.64	19.61
LSTM	0.991	0.989	10.27	28.77
Proposed	0.995	0.995	4.81	8.59

proposed method consistently outperforms SKF. In contrast, Semi-CC-GT suffers a significant accuracy drop under sparse measurements and gradually improves as M increases, indicating strong dependence on dense measurements.

B. Generalization to Discontinuous Trajectories

This section demonstrates that the proposed model generalizes well to discontinuous trajectories of varying lengths, effectively handling irregular path segments.

To this end, over 10,000 randomly generated trajectories of varying lengths, ranging from 200 m to 1,000 m, are used for training, with an additional 100 trajectories for evaluation. We also benchmark the proposed model against a conventional long short-term memory (LSTM) architecture by replacing the RNN–CNN block with the LSTM structure while keeping all other configurations unchanged.

The generalization results for 40 trajectory samples are show in Fig. 8, and the positioning accuracy comparison is summarized in Table II. It is observed that the proposed method consistently outperforms all baselines, achieving roughly 0.005 higher TW and CT scores and more than a 2.5 m improvement in localization accuracy. Compared with the LSTM baseline, it improves localization accuracy by 53% and reduces the 95th-percentile error by 70%.

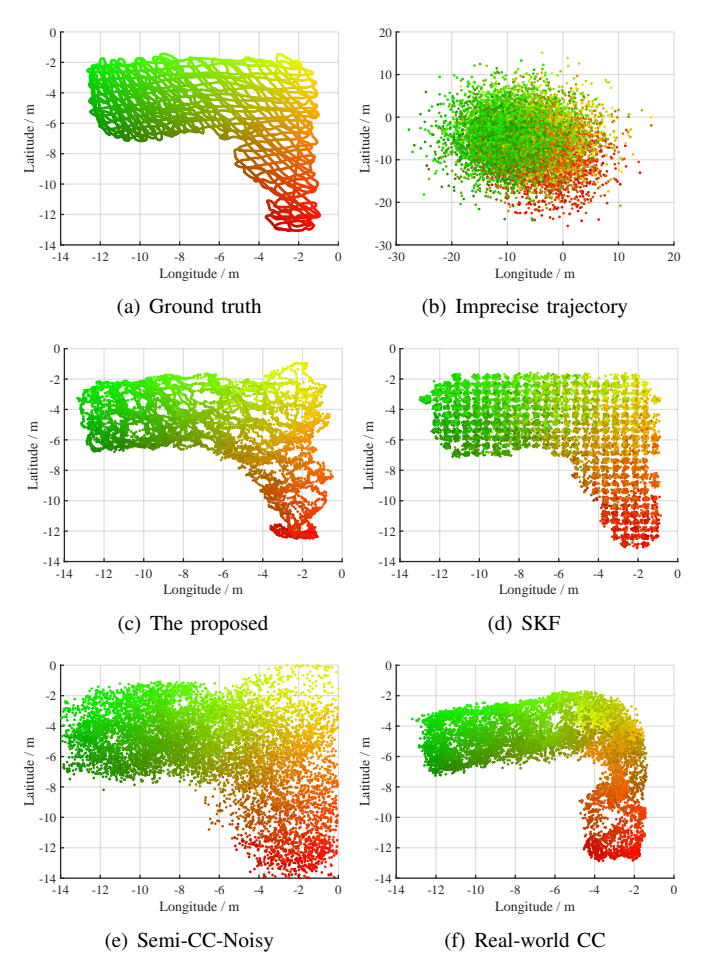


Figure 9. Trajectory recovery results for the measured indoor scenario.

As shown in Fig. 8, the trajectories generated by the proposed method are smooth and continuous, and align most closely with the ground truth. The results of LSTM and Semi-CC-GT exhibit noticeable local fluctuations and larger variance. Notably, each trajectory of LSTM shows significant deviation at the beginning segment. This is because recurrent structures have limited past context at early time steps, resulting in poor memory initialization and large early prediction errors. In contrast, the proposed model effectively overcomes this issue, which demonstrates the robustness of our design and its superior generalization ability to more complex scenarios.

C. Trajectory Recovery for Indoor Scenario

We further demonstrate that the proposed model performs robustly in the measurement-based indoor scenario, maintaining consistent performance across diverse environments.

In this experiment, the radio map grid resolution is set to 0.5 meters, and the loss weights are configured as $\lambda_c = 0.01$, $\lambda_t = 5$ and $\lambda_d = 2$. The imprecise trajectory $\{\bar{\mathbf{p}}_r^l\}_{l=1}^L$ is generated by adding Gaussian noise with variance $\sigma^2 = 25$.

Fig. 9 shows the ground truth and predicted trajectories of the compared methods. As seen in Fig. 9(b), the initial imprecise trajectory is fully corrupted by noise, obscuring positional information and making direct localization highly difficult. While all methods can roughly classify sample

Table III Positioning Performance Comparison for Indoor Scenario

	Latent Space Quality		Positioning Error / m	
Scheme	TW↑	СТ ↑	Mean ↓	95th Percentile ↓
SKF	0.847	0.886	1.56	3.19
Semi-CC-Noisy	0.975	0.983	0.76	1.63
Real-world CC	0.969	0.988	0.99	2.28
Proposed	0.991	0.992	0.49	1.08

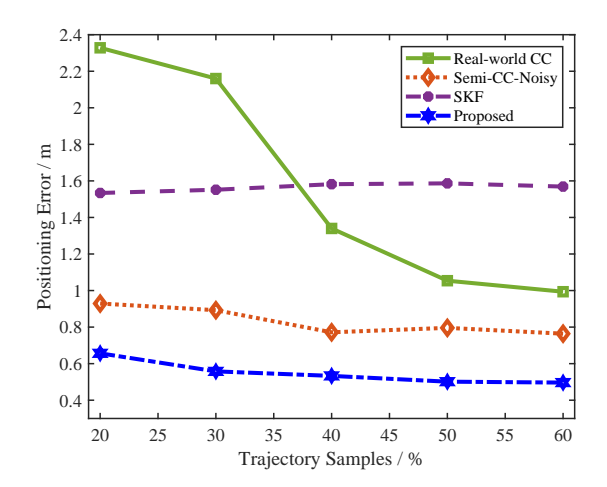


Figure 10. Positioning error versus the ratio of trajectory samples.

points within the green-to-red gradient area, only the proposed method consistently preserves trajectory continuity and smoothness, closely matching the true trajectory, whereas the baselines produce scattered clusters that may lack the temporal coherence of true trajectories.

Table III summarizes the localization accuracy comparison for the indoor scenario. It is observed that the proposed model consistently outperforms all baselines across all metrics, with TW and CT scores improving by at least 0.01. For real-world localization, it reduces localization error by 35.1% to 68.3% and the 95th-percentile error by 32.9% to 66.1%, indicating robust performance even in worst-case scenarios. Notably, Real-world CC outperforms SKM here, likely due to slow channel variations and dominant LOS conditions indoors.

In addition, we evaluate positioning error across various trajectory sample ratios from 20% to 60% of the indoor dataset. Fig. 10 shows that the proposed method consistently outperforms all baselines across all sample proportions. As the number of samples increases, errors decrease for all methods except SKM, which remains nearly unchanged. Real-world CC improves significantly when the sample ratio exceeds 50% but performs worse than SKM below 40%, indicating a high data requirement. In contrast, the proposed method maintains high localization accuracy even with limited samples, which demonstrates robustness and efficiency in data-scarce scenarios and thus reducing the practical data collection burden.

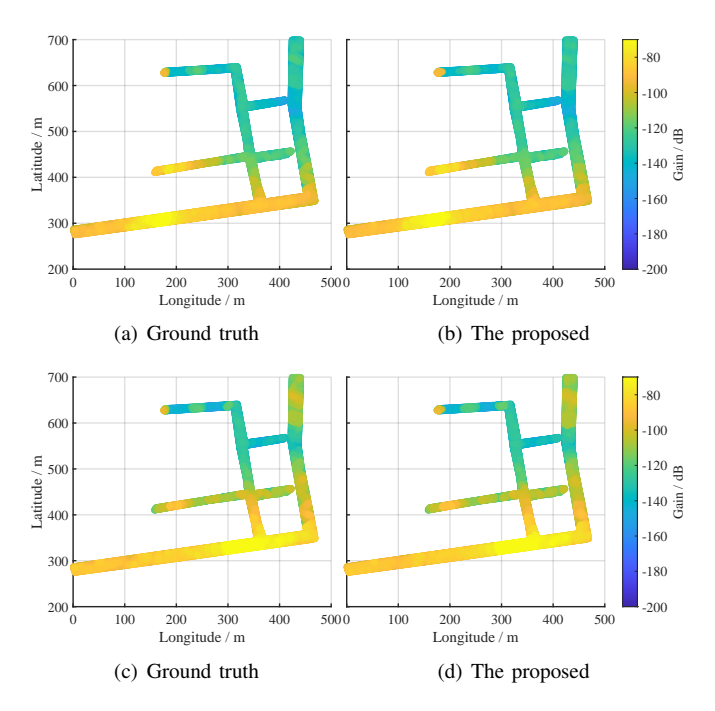


Figure 11. MIMO beam map of BS1 for specific beam directions: a) and c) The ground truth; b) and d) The beam map generated by the proposed model.

Table IV Comparison Results of Radio Map Construction.

	The number of CSI measurement			
Scheme	M=1	M=3	M=5	
		NMAE / RMSE		
SKF	0.013 / 0.068	0.012 / 0.067	0.012 / 0.067	
Proposed	0.0062 / 0.050	0.0056 / 0.047	0.0049 / 0.044	

D. Radio Map construction

We evaluate the performance of the proposed model in constructing MIMO beam maps from sparse CSI measurements.

Fig. 11 shows the MIMO beam maps of BS1 under two beam directions along the main road of the city. In dense urban areas, radio geometry is highly complex due to numerous obstacles. The results demonstrate that the proposed model accurately reconstructs the radio beam geometry, such as beam shape, direction, blockage, and reflections. The close match with ground truth indicates high-fidelity channel generation from the learned radio map embedding. Notably, in Fig. 11(c) and (d), despite irregular multipath and reflections along the left road, the proposed method still successfully reproduces the complex beam patterns and spatial energy distribution.

In addition, Table IV summarizes the radio map reconstruction performance in terms of NMSE and RMSE under varying numbers of CSI measurements (i.e., M=1,3, and 5). As the CSI number M increases, the accuracy of the proposed method improves, while SKF remains largely unchanged. Notably, even with M=1, the proposed method outperforms SKF, reducing NMSE by 52.3% and RMSE by 26.5%. With M=5, NMSE and RMSE further decrease by 59.1% and 34.3%, respectively. These results demonstrate

that the proposed method can accurately reconstruct MIMO beam maps and generate full CSI from extremely sparse CSI measurements, even with just a single CSI measurement per BS at each UE locition, which demonstrates its robustness in scenarios with highly limited channel measurements.

E. Radio-Map-Embedded Beam Tracking

This section shows the real-time application of the proposed deep learning method for radio-map-embedded beam tracking.

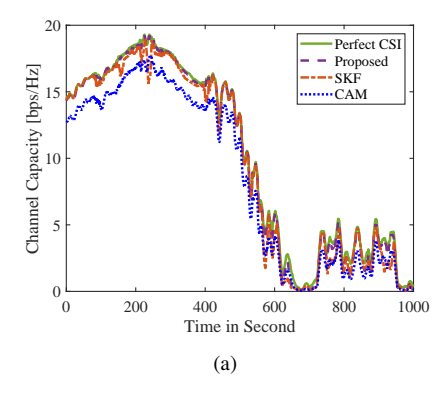
In this experiment, we account for varying signal-to-noise ratios (SNRs), where the SNR is defined as SNR = $P_t\mathbb{E}[|\mathbf{h}(\tilde{\mathbf{p}})\mathbf{w}|^2]/\sigma_n^2$ based on the mean channel power and the given noise variance. For evaluation, we employ the outdoor dataset to perform beam tracking, and parameters kept consistent with Section IV-A.

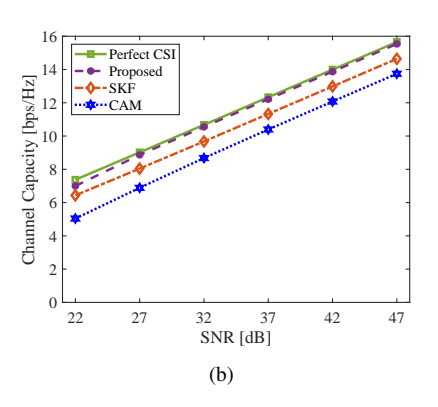
Fig. 12(a) shows the real-time channel capacity along a trajectory from LOS to NLOS regions. The results indicate that the channel exhibits temporal fluctuations, and all methods generally capture these variations with trends close to the perfect CSI. Among them, the proposed method most closely matches the perfect CSI with minimal deviations, followed by SKF and CAM. Notably, the proposed method consistently outperforms both SKF and CAM in LOS and NLOS regions.

Fig. 12(b) and (c) illustrate the average channel capacity along trajectories under LOS and NLOS conditions, respectively. While all methods show improved channel capacity with increasing SNR, the proposed method consistently outperforms the baselines, which achieves performance closest to the perfect CSI, reaching up to 98% of the ideal channel capacity in LOS condition and maintaining an approximately 77.5% even in challenging NLOS condition. By contrast, while SKF reaches 97% of the perfect CSI channel capacity in LOS condition, but drops to only 57% in NLOS regions. The advantage of the proposed method in NLOS condition becomes more pronounced at higher SNRs, improving channel capacity over SKF by 25.1% at SNR = -11 dB and up to 35.4% at SNR = 6 dB.

V. CONCLUSION

This paper developed a deep radio-map-embedded generative framework for joint trajectory recovery and MIMO beam map reconstruction using sequences of sparse CSI measurements without explicit location labels. To mitigate the uncertainty of highly sparse CSI, a dual-scale feature extraction scheme that integrated with self-attention and multiscale convolutions was designed to enhance feature representation by exploiting angular correlations within each CSI snapshot and spatial correlations across neighboring samples. We developed a hybrid RNN-CNN encoder to capture mobility patterns, incorporating a truncation strategy and multi-scale convolutions in the RNN to enhance robustness against shortterm fluctuations. Unlike conventional Gaussian priors, we embedded a learnable radio map in the latent space to capture location information by encoding high-level positional features from CSI, and employed a DDPM based generative decoder to reconstruct full CSI with high fidelity conditioned on the positional features. Design examples showed that the proposed





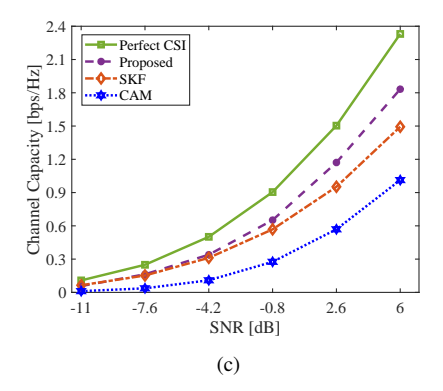


Figure 12. Beam tracking performance. a) Channel capacity for a trajectory transitioning through LOS and NLOS propagation conditions to BS1; b) Channel capacity for LOS trajectories to BS2; c) Channel capacity for NLOS trajectories to BS3.

model can improve localization accuracy by over 30% and channel capacity gain by 20% in NLOS scenarios compared to Kalman filter methods.

REFERENCES

- [1] Y. Zeng, J. Chen, J. Xu, D. Wu, X. Xu, S. Jin, X. Gao, D. Gesbert, S. Cui, and R. Zhang, "A tutorial on environment-aware communications via channel knowledge map for 6G," *IEEE Commun. Surv. Tutorials.*, vol. 26, no. 3, pp. 1478–1519, 2024.
- [2] H. Peng, T. Kallehauge, M. Tao, and P. Popovski, "Fast transmission control adaptation for URLLC via channel knowledge map and metalearning," *IEEE Internet Things J.*, vol. 12, no. 9, pp. 13097–13111, 2025
- [3] C. He, Y. Dong, and Z. J. Wang, "Radio map assisted multi-UAV target searching," *IEEE Trans. Wireless Commun.*, vol. 22, no. 7, pp. 4698– 4711, 2023.
- [4] Q. Xue, C. Ji, S. Ma, J. Guo, Y. Xu, Q. Chen, and W. Zhang, "A survey of beam management for mmwave and THz communications towards 6G," *IEEE Commun. Surv. Tutor.*, vol. 26, no. 3, pp. 1520–1559, 2024.
- [5] D. Wu, Y. Zeng, S. Jin, and R. Zhang, "Environment-aware hybrid beamforming by leveraging channel knowledge map," *IEEE Trans. Wireless Commun.*, vol. 23, no. 5, pp. 4990–5005, 2024.
- [6] W. B. Chikha, M. Masson, Z. Altman, and S. B. Jemaa, "Radio environment map based inter-cell interference coordination for massive-MIMO systems," *IEEE Trans. Mob. Comput.*, vol. 23, no. 1, pp. 785– 796, 2024.
- [7] Y. Hu and R. Zhang, "A spatiotemporal approach for secure crowd-sourced radio environment map construction," *IEEE/ACM Trans. Netw.*, vol. 28, no. 4, pp. 1790–1803, 2020.
- [8] N. Dal Fabbro, M. Rossi, G. Pillonetto, L. Schenato, and G. Piro, "Model-free radio map estimation in massive MIMO systems via semiparametric Gaussian regression," *IEEE Wireless Commun. Lett.*, vol. 11, no. 3, pp. 473–477, 2022.
- [9] C. Phillips, M. Ton, D. Sicker, and D. Grunwald, "Practical radio environment mapping with geostatistics," in *Proc. IEEE Int. Symp. Dyn. Spectr. Access Netw.*, 2012, pp. 422–433.
- [10] Y. Zhang and S. Wang, "K-Nearest neighbors Gaussian process regression for urban radio map reconstruction," *IEEE Commun. Lett.*, vol. 26, no. 12, pp. 3049–3053, 2022.
- [11] H. Sun and J. Chen, "Integrated interpolation and block-term tensor decomposition for spectrum map construction," *IEEE Trans. Signal Process.*, vol. 72, pp. 3896–3911, 2024.
- [12] G. Zhang, X. Fu, J. Wang, X.-L. Zhao, and M. Hong, "Spectrum cartography via coupled block-term tensor decomposition," *IEEE Trans. Signal Process.*, vol. 68, pp. 3660–3675, 2020.
- [13] S. Zhang, A. Wijesinghe, and Z. Ding, "RME-GAN: A learning framework for radio map estimation based on conditional generative adversarial network," *IEEE Internet Things J.*, vol. 10, no. 20, pp. 18016–18027, 2023.
- [14] W. Chen and J. Chen, "Diffraction and scattering aware radio map and environment reconstruction using geometry model-assisted deep learning," *IEEE Trans. Wireless Commun.*, vol. 23, no. 12, pp. 19804– 19819, 2024.

- [15] H. Jia, N. Cheng, X. Wang, C. Zhou, R. Sun, and X. Shen, "Ra-dioMamba: Breaking the accuracy-efficiency trade-off in radio map construction via a hybrid Mamba-UNet," *IEEE Transactions on Network Science and Engineering*, pp. 1–14, 2025, Early Access.
- [16] X. Wang, K. Tao, N. Cheng, Z. Yin, Z. Li, Y. Zhang, and X. Shen, "Radiodiff: An effective generative diffusion model for sampling-free dynamic radio map construction," *IEEE Trans. Cognit. Commun. Netw.*, vol. 11, no. 2, pp. 738–750, 2025.
- [17] X. Luo, Z. Li, Z. Peng, M. Chen, and Y. Liu, "Denoising diffusion probabilistic model for radio map estimation in generative wireless networks," *IEEE Trans. Cogn. Commun. Netw.*, vol. 11, no. 2, pp. 751– 763, 2025.
- [18] D. He, B. Ai, K. Guan, L. Wang, Z. Zhong, and T. Kürner, "The design and applications of high-performance ray-tracing simulation platform for 5G and beyond wireless communications: A tutorial," *IEEE Commun. Surv. Tutor.*, vol. 21, no. 1, pp. 10–27, 2019.
- [19] N. Suga, R. Sasaki, M. Osawa, and T. Furukawa, "Ray tracing acceleration using total variation norm minimization for radio map simulation," *IEEE Wirel. Commun. Lett.*, vol. 10, no. 3, pp. 522–526, 2021.
- [20] P. Kazemi, H. Al-Tous, T. Ponnada, C. Studer, and O. Tirkkonen, "Beam SNR prediction using channel charting," *IEEE Trans. Veh. Technol.*, vol. 72, no. 10, pp. 13130–13145, 2023.
- [21] C. Studer, S. Medjkouh, E. Gonultas, T. Goldstein, and O. Tirkkonen, "Channel charting: Locating users within the radio environment using channel state information," *IEEE Access*, vol. 6, pp. 47682–47698, 2018.
- [22] Q. Zhang and W. Saad, "Semi-supervised learning for channel chartingaided IoT localization in millimeter wave networks," in *Proc. IEEE Glob. Commun. Conf. (GLOBECOM)*, 2021, pp. 1–6.
- [23] I. Karmanov, F. G. Zanjani, I. Kadampot, S. Merlin, and D. Dijkman, "Wicluster: Passive indoor 2D/3D positioning using WiFi without precise labels," in *Proc. IEEE Glob. Commun. Conf. (GLOBECOM)*, 2021, pp. 1–7.
- [24] M. Stahlke, G. Yammine, T. Feigl, B. M. Eskofier, and C. Mutschler, "Indoor localization with robust global channel charting: A time-distance-based approach," *IEEE Trans. on Mach. Learn. in Commun. and Netw.*, vol. 1, pp. 3–17, 2023.
- [25] S. Taner, V. Palhares, and C. Studer, "Channel charting in real-world coordinates with distributed MIMO," *IEEE Trans. Wireless Commun.*, vol. 24, no. 9, pp. 7286–7300, 2025.
- [26] Y. Zheng and J. Chen, "A radio map approach for reduced pilot CSI tracking in massive MIMO networks," *IEEE Trans. Signal Process.*, vol. 73, pp. 2833–2847, 2025.
- [27] K. Magowe, A. Giorgetti, S. Kandeepan, and X. Yu, "Accurate analysis of weighted centroid localization," *IEEE Trans. Cogn. Commun. Netw.*, vol. 5, no. 1, pp. 153–164, 2019.
- [28] A. Razavi, A. van den Oord, and O. Vinyals, "Generating diverse high-fidelity images with VQ-VAE-2," in *Proc. Adv. Neural Inf. Process. Syst.* (NeurIPS), vol. 32, 2019.
- [29] F. Euchner and M. Gauger, "CSI dataset dichasus-cf0x: Distributed antenna setup in industrial environment, day 1," 2022. [Online]. Available: https://doi.org/doi:10.18419/darus-2854.
- [30] D. Wu and Y. Zeng, "Environment-aware coordinated multi-point mmwave beam alignment via channel knowledge map," in *Proc. IEEE Int. Conf. Commun. (ICC)*, 2023, pp. 1044–1049.